Kim et al. *NPG Asia Materials* (2023) 15:32
https://doi.org/10.1038/s41427-023-00480-1

NPG Asia Materials

REVIEW ARTICLE Open Access

Aggregates of conjugated polymers: bottom-up control of mesoscopic morphology and photophysics

Chanwoo Kim[1], Hyeyoung Joung[1], Hyung Jun Kim[2], Keewook Paeng[3], Laura J. Kaufman[2] and Jaesung Yang[1]

Abstract

Conjugated polymer (CP) aggregates have been the focus of considerable research, as these mesoscopic entities, compared with single CP chains, provide environments more analogous to those present in polymer-based optoelectronics in terms of the complexity of morphology and chain interactions; thereby, such aggregates hold the potential to provide insights into structure–function relationships highly relevant to optoelectronic device efficiency and stability. This review article highlights single-aggregate spectroscopy studies of CP aggregates based on a combination of solvent vapor annealing and single-molecule fluorescence techniques and draws mesoscopic connections between morphology, electronic coupling, and photophysics in CPs. This molecular-level understanding will pave the way for the bottom-up control of optoelectronic properties from the molecular to the device-length scale.

Introduction

Conjugated polymers (CPs) have been the subject of considerable research owing to their potential as organic semiconductors in optoelectronic devices, such as organic light-emitting diodes, organic transistors, and solar cells[1–15]. The major advantages of CP usage in such devices include solution processability, synthetic versatility, mechanical flexibility, and tunable photophysical properties[16–27]. Despite their exceptional potential in modern optoelectronics, reaching a fundamental understanding of the relationship between CP morphology and photophysics remains a critical and challenging problem due to the inherent complexity of thin-film device morphology across a wide variety of length scales. While individual CPs have been studied over the last two to three decades, CP aggregates have become a more recent focus of research, facilitating insights into the structure–function relationship at the mesoscopic length scale[28–35]. Such studies are of substantial interest for several reasons: first, compared with an isolated single chain, mesoscopic aggregates better replicate the structural and electronic complexity present in densely packed environments in which multiple chains coexist in close proximity and strongly interact with each other; second, the introduction of a new experimental framework involving the solvent vapor annealing (SVA) of a host matrix film containing CPs of interest has enabled the formation of CP aggregates that are sufficiently isolated from each other, allowing the utilization of established single-molecule techniques to investigate aggregate morphology and photophysics on an aggregate-to-aggregate basis[36–44].

This review article describes the general relationship between mesoscopic morphology, electronic coupling, and photophysics in CPs as established via single-aggregate spectroscopy of CP aggregates. In the following sections, we describe the SVA-based methodology for preparing isolated aggregates in thin films, advances in associated techniques, mechanisms contributing to aggregate formation and growth, the relationship of nanoscale morphology with

Correspondence: Keewook Paeng (paeng@skku.edu) or
Laura J. Kaufman (kaufman@chem.columbia.edu) or
Jaesung Yang (jaesung.yang@yonsei.ac.kr)
[1]Department of Chemistry, Yonsei University, Wonju, Gangwon 26493, Korea
[2]Department of Chemistry, Columbia University, New York, NY 10027, USA
Full list of author information is available at the end of the article
These authors contributed equally: Chanwoo Kim, Hyeyoung Joung

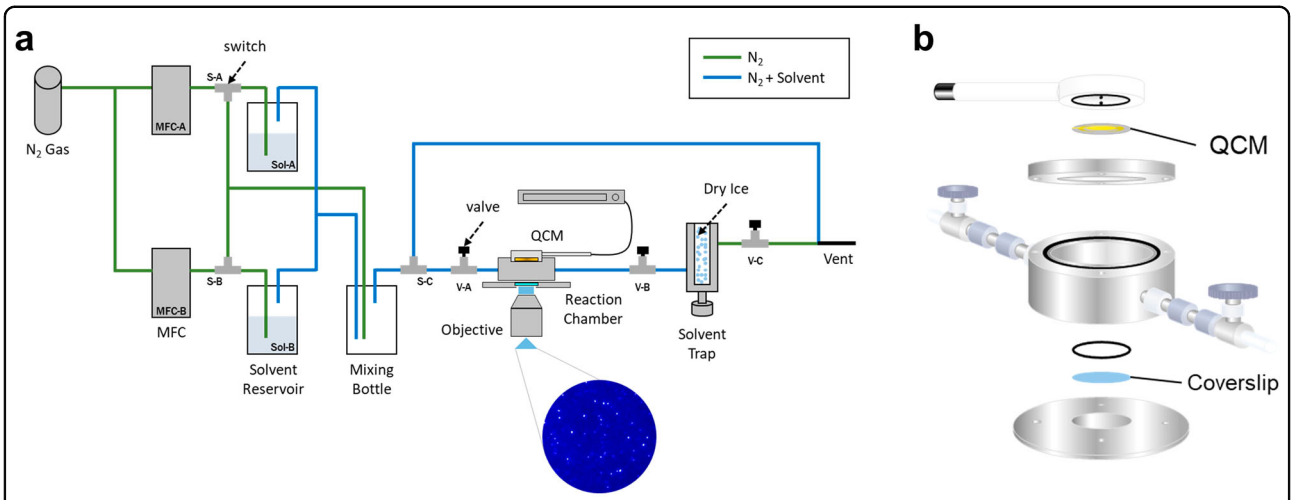

Fig. 1 Design of a multimodal apparatus to study CP aggregates. a Schematic diagram of an SVA system including MFCs, solvent reservoirs, a sample chamber, and QCM. Reproduced with permission from ref. [47]. Copyright 2016 American Institute of Physics (AIP) Publishing. **b** Schematic diagram of a custom-built sample chamber with QCM. Reproduced with permission from ref. [123]. Copyright 2022 American Chemical Society.

intrachain and interchain interactions, factors affecting the morphological order of aggregates, synthetic strategies for the tailoring of aggregate morphology, photophysics of aggregates distinct from single chains, and finally, SVA studies of single polymers and oligomers.

SVA-based methodology for preparing CP aggregates

In 2011, Barbara and colleagues established a straightforward SVA-based methodology to fabricate CP aggregates from single-chain CPs in thin films[45]. They prepared a film composed of single chains of the paradigmatic CP poly(2-methoxy-5-(2'-ethylhexyloxy)-1,4-phenylene-vinylene) (MEH-PPV) dispersed in an inert host matrix, poly(methyl methacrylate) (PMMA), with an MEH-PPV concentration approximately 50 times higher than that used in typical single-chain studies. For SVA of the film, an acetone-chloroform solvent vapor mixture was used: acetone is a poor solvent for the CP, with the polymer–solvent interaction parameter χ being > 0.5, while $\chi < 0.5$ for the host matrix; in contrast, chloroform is a nonselective good solvent, where $\chi < 0.5$ for both the CP and host matrix[46]. The use of this binary mixture is essential for initiating the aggregation of CPs because the process relies largely on Ostwald ripening, a process described further in Section 3. Swelling the MEH-PPV/PMMA blended film with the acetone–chloroform solvent vapor mixture allowed the diffusion of single CP chains, triggering the formation and growth of CP aggregates. Upon film deswelling, the resulting aggregates were effectively isolated from one another, thereby enabling them to be interrogated on an individual basis using established single-particle techniques.

Although SVA is a simple technique, precise control of the degree and time course of film swelling by regulating process parameters, such as vapor flow rate and vapor pressure, has proven challenging. Nevertheless, achieving this is essential for fabricating CP aggregates with the desired morphology and properties and ensuring experimental reproducibility. Kaufman and colleagues developed a multimodal apparatus with an ingenious design, as illustrated in Fig. 1[47]. This design incorporates a chamber in which a sample film is mounted on a quartz crystal microbalance (QCM), allowing the real-time monitoring of the swelling degree of the film throughout the SVA process, while another equivalent film on a glass coverslip is subjected to single-particle fluorescence microscopy. In addition, a solvent vapor delivery system consisting of a series of mass-flow controllers (MFCs) allows direct and rapid control of the process parameters. The authors demonstrated that this apparatus affords enhanced control over the SVA process and, in turn, the characteristics of CP aggregates, such as size, morphology, photophysics, and growth mechanism.

Mechanism of aggregate growth

It was initially proposed that CP aggregate growth occurred through Ostwald ripening[48–51]. This is a thermodynamically driven, spontaneous process in which single CP chains preferentially dissolve from smaller aggregates and redeposit onto larger ones. The minimum size of stable aggregates is predetermined by the critical radius R_c, which can be expressed as follows[52]:

$$R_c = \left(\frac{2\sigma}{kT}\right) v \frac{C_\infty}{C - C_\infty} \text{ for } C_\infty < C$$

where C is the CP concentration and C_∞ is the saturation concentration of the CP regarding the solvent-swollen host matrix as the solvent. This equation suggests that aggregate size can be modulated by adjusting C_∞ while C remains constant. This can be achieved by altering the vapor volume ratio of the good–poor-solvent mixture, V_g/V_p, as C_∞ increases with an increase in V_g/V_p (Fig. 2a). Indeed, the SVA of MEH-PPV/PMMA films using chloroform-acetone solvent mixtures with different V_g/V_p values led to the formation of MEH-PPV aggregates of different sizes, as assessed by single-aggregate fluorescence intensity (Fig. 2b). In particular, the size and number of aggregates per imaging area were anti-correlated as a function of V_g/V_p (Fig. 2c), which agrees with predictions indicating Ostwald ripening.

Yang et al. performed in situ real-time observations of CP aggregate growth, showing that it indeed occurs through multiple mechanisms[53]. To track the dynamic growth of individual aggregates in solvent swollen films, they performed in situ optical imaging by recording a series of videos over the course of the SVA of MEH-PPV/PMMA films. MEH-PPV aggregates exhibited two types of anti-correlated temporal changes in fluorescence intensity and diffusivity: growing aggregates gradually became brighter and slower, whereas dissipating aggregates exhibited the opposite behavior (Fig. 3a). This dual observation directly evinced Ostwald ripening as an operative mechanism in aggregate growth. Surprisingly, during this aggregate growth process, particular aggregates underwent repetitive approaching–receding events, and a small portion coalesced to form a single larger aggregate (Fig. 3b). This previously undescribed process was responsible for nearly half of the decrease in aggregate number that occurred over the duration of the videos, while the remainder was attributed to Ostwald ripening, confirming the importance of both mechanisms in CP aggregate growth.

Electronic coupling in CP aggregates

Electronic coupling in CP aggregates plays a decisive role in determining their photophysics[54–60]. A theoretical framework to illustrate coupling mechanisms was constructed by Spano et al.[61–68] and is thoroughly outlined in the introductory section of ref. [69]. Briefly, J-type coupling arises from intrachain interactions between covalently linked repeat units within a single CP. This coupling becomes stronger if more repeat units are coupled or if the coupling strength increases upon backbone planarization. The S_1-S_0 transition is dipole-allowed, and thus, a J-type-coupled system is expected to exhibit spectroscopic changes such as spectral redshifts, narrowing of the 0-0 vibronic transition, an increase in the 0-0 to 0-1 vibronic peak ratio ($I_{0\text{-}0/0\text{-}1}$), and a decrease in fluorescence lifetime (τ_F) in comparison to an uncoupled system. In contrast, H-type coupling mainly arises from interchain interactions between nearby cofacial chains on different CPs.

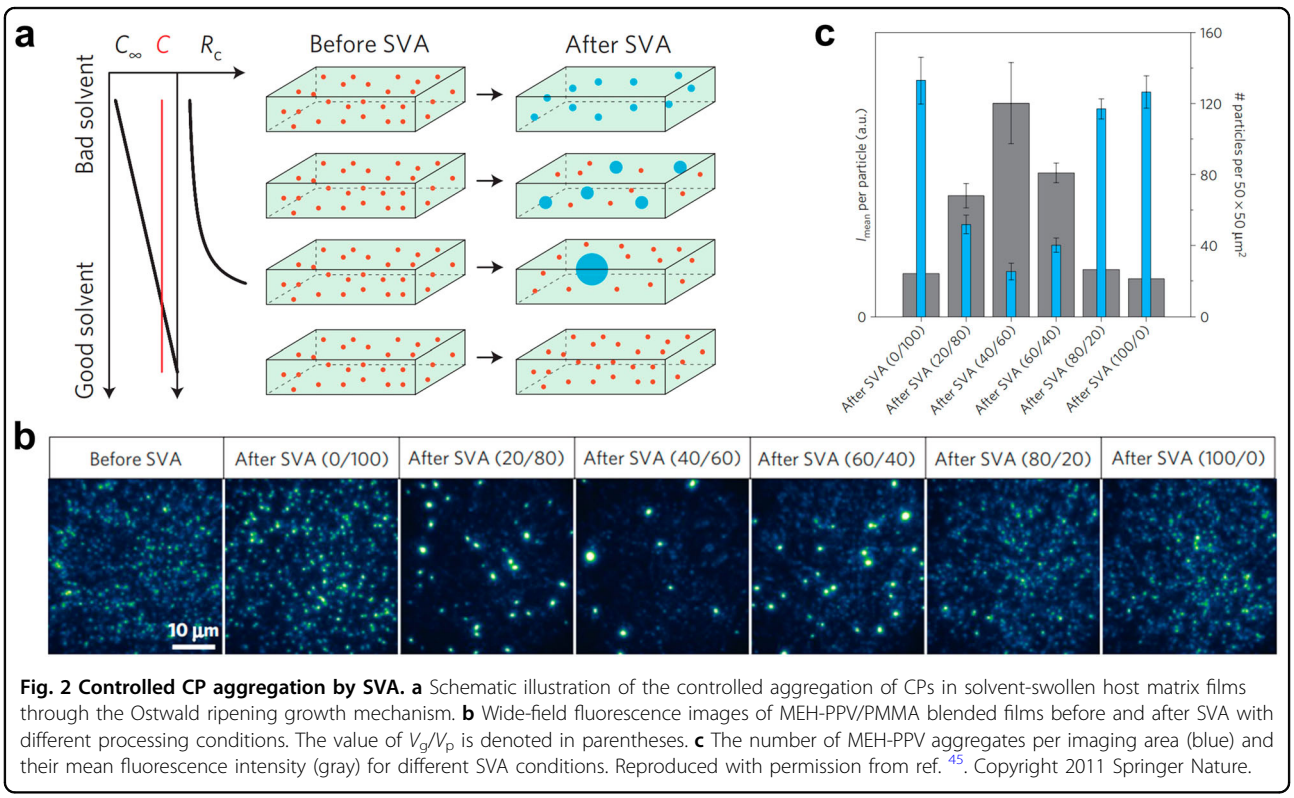

Fig. 2 Controlled CP aggregation by SVA. a Schematic illustration of the controlled aggregation of CPs in solvent-swollen host matrix films through the Ostwald ripening growth mechanism. **b** Wide-field fluorescence images of MEH-PPV/PMMA blended films before and after SVA with different processing conditions. The value of V_g/V_p is denoted in parentheses. **c** The number of MEH-PPV aggregates per imaging area (blue) and their mean fluorescence intensity (gray) for different SVA conditions. Reproduced with permission from ref. [45]. Copyright 2011 Springer Nature.

In principle, the S_1–S_0 transition here is dipole-forbidden, and thus, the associated spectroscopic changes for an H-type-coupled system should be opposite to those of a J-type-coupled system. The described framework based on J- and H-type coupling highlights the intimate correlation between electronic coupling and chain morphology in CP aggregates; high degrees of intrachain and interchain ordering are respectively required for effective J- and H-type coupling to occur.

Vogelsang et al. experimentally validated this correlation using poly(*para*-phenylene-ethynylene-butadiynylene) (PPEB) derivatives with different side chains: PPEB-1, PPEB-2, and PPEB-3 bore hexyloxy-, 2-ethylhexyloxy-, and cholestenol-substituted benzyloxy side chains, respectively (Fig. 4a, b)[69]. Single chains of PPEB-1, PPEB-2, and PPEB-3 showed no difference in fluorescence in terms of spectral position and width, $I_{0\text{-}0/0\text{-}1}$, or τ_F; however, isolated aggregates thereof prepared via SVA showed very different behaviors depending on the side chains (Fig. 4c, d). Specifically, the PPEB-1 aggregates exhibited spectroscopic characteristics typical of H-type coupling, including decreased $I_{0\text{-}0/0\text{-}1}$ and enhanced τ_F compared to those for the corresponding single chains. This phenomenon was attributed to the well-ordered aggregate morphology as assessed by excitation polarization fluorescence spectroscopy. The spectral widths of the PPEB-1 aggregates were broadly distributed, reflecting different degrees of coupling due to variations in interchain separation within aggregates. In stark contrast, the PPEB-2 aggregates exhibited a narrowed, redshifted 0-0

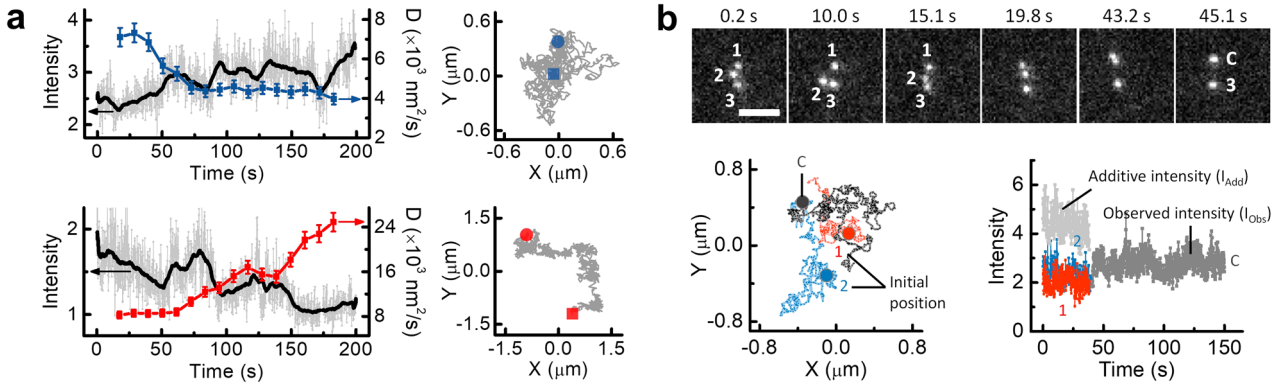

Fig. 3 In situ observation of aggregate growth. a At left, fluorescence intensity (gray), smoothed fluorescence intensity (black), and diffusion coefficients (blue and red) of growing (top) and dissipating (bottom) MEH-PPV aggregates. Shown at right are the corresponding two-dimensional trajectories. **b** Time-lapse fluorescence images showing aggregate coalescence: MEH-PPV aggregates **1** and **2** merge to form aggregate **C**. Shown below are the corresponding two-dimensional trajectories (left) and fluorescence intensity trajectories (right). Reproduced with permission from ref. [53]. Copyright 2018 John Wiley and Sons.

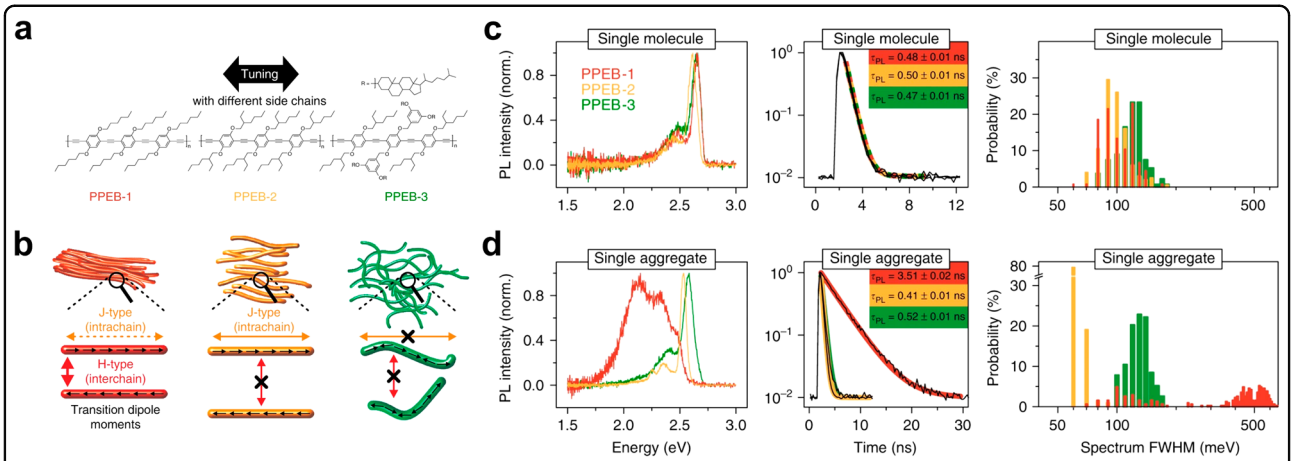

Fig. 4 Electronic coupling in CP aggregates. a Structures of PPEB-1, PPEB-2, and PPEB-3. **b** Types of electronic coupling (H- and J-type or the inhibition of coupling) depending on aggregate morphology. **c**, **d** Normalized fluorescence spectra (left), normalized time-resolved fluorescence decays (middle), and spectrum full width at half maximum (FWHM) values (right) for single molecules and single aggregates of PPEB-1, PPEB-2, and PPEB-3. Reproduced with permission from ref. [69]. Copyright 2017 Springer Nature.

peak, an increased $I_{0\text{-}0/0\text{-}1}$, and a shortened τ_F, demonstrating the emergence of J-type coupling upon CP aggregation. No electronic coupling occurred in the PPEB-3 aggregates because of the bulky side chains, as evidenced by the spectroscopic similarity between single chains and aggregates of PPEB-3.

A hierarchy was observed in electronic coupling with regard to the manifestation of spectroscopic characteristics. Isolated aggregates of PPEB-1 initially exhibited typical spectroscopic characteristics of H-type coupling in the dried film, later exhibited the characteristics of J-type coupling after gentle swelling of the film, and finally recovered their initial characteristics after film deswelling. This observation can be explained as follows: in the swollen film, aggregate swelling leads to an increase in interchain separation within aggregates, thus selectively interrupting interchain H-type coupling and revealing spectroscopic evidence of intrachain J-type coupling. From this reversible switching of electronic coupling, it was suggested that interchain H-type coupling can completely mask intrachain J-type coupling when the two types coexist in CP aggregates.

Engineering of aggregate morphology

As described in the previous section, the highly ordered anisotropic morphology of CP aggregates is essential for robust intrachain and interchain interactions through J- and H-type couplings, which can facilitate long-range exciton transport across mesoscopic length scales. In this section, we review the factors affecting the morphological order of CP aggregates and strategies to engineer CP aggregate morphology for the enhancement of exciton transport properties.

The most common method for assessing the degree of morphological order of individual CP aggregates is polarization modulation depth (M) measurements[70]. In these measurements, the single-aggregate fluorescence intensity (I) is measured as a function of the polarization angle (ϕ) of linearly polarized excitation light. M is expressed as $I(\phi) = I_0[1 + M\{2(\phi - \phi_0)\}]$, where I_0 and ϕ_0 denote the average intensity and the reference polarization angle corresponding to the maximum intensity, respectively. An aggregate with highly aligned chromophores will behave as an anisotropic absorber and show an M value close to 1, whereas disorder in the arrangement of chromophores will lead to M values close to 0.

CP aggregates have been shown to preserve morphological characteristics templated by single-chain building blocks[71–75]. It is widely accepted that MEH-PPV initially dissolved in toluene (a poor solvent for the CP) and dispersed in inert host matrices adopts a highly ordered anisotropic conformation at the single-molecule level, while MEH-PPV initially dissolved in chloroform, a good solvent for the CP, adopts a poorly ordered, relatively isotropic conformation. The Kaufman group showed that these initial chain conformations remained unchanged following SVA, as evidenced by the small difference in median M values before and after SVA (Fig. 5b–i)[76,77]. Consistent with the conformational order of the single-chain templates, MEH-PPV aggregates of three different sizes prepared using toluene as the initial dissolving solvent maintained fairly high M values with a median $M = 0.67$ for the largest aggregates. In contrast, those prepared using chloroform exhibited a decrease in the median M value to 0.16 with increasing aggregate size. This confirmed that single-chain templates play an essential role in determining the morphological order of CP aggregates. The two aggregate growth mechanisms described in Section 3 had a distinct impact on the evolution of the morphological order of the growing aggregates. The growth of MEH-PPV aggregates via Ostwald ripening preserved the anisotropic morphology templated on single chains with a collapsed and ordered conformation. In contrast, aggregate coalescence primarily occurred with no preferential direction, although two coalescing aggregates initially displayed a highly anisotropic morphology, leading to a notable reduction in the degree of aggregate anisotropy[53].

Chemical modification of polymer structures has been shown to be an effective method for engineering aggregate morphology[78–82]. To make the chain backbone more linear or kinked, Vanden Bout et al. modified the prototypical CP MEH-PPV such that 30% of the monomers were replaced by backbone-directing *para*- and *ortho*-terphenyl inclusions (Fig. 5j)[83]. Compared to aggregates formed from pristine MEH-PPV, those of *para*-terphenyl-containing MEH-PPV displayed a more highly ordered morphology, as indicated by an increase in mean M from 0.42 to 0.76. In contrast, aggregates of *ortho*-terphenyl-containing MEH-PPV displayed a nearly isotropic morphology, with a mean M of 0.18. As an alternative strategy for extending the backbone conformation, Hu et al. introduced fluorine atoms into the chain backbone of poly(3-ethylhexylthiophene) (P3EHT), which yielded poly(3-ethylhexyl-4-fluorothiophene) (F-P3EHT)[84]. Molecular dynamics simulations and M measurements of these CP single chains revealed that backbone fluorination dramatically altered the chain conformation from random-coil-like for P3EHT to extended-rod-like for F-P3EHT. Consistent with the findings of the Kaufman group described above, the ordered single-chain template of F-P3EHT facilitated the formation of aggregates with a high degree of morphological ordering, as evident from the high M values (Fig. 5k). In addition to backbone tailoring, side chain substitution has been shown to impact aggregate morphology[85–92]. Hu et al. prepared three types of aggregates

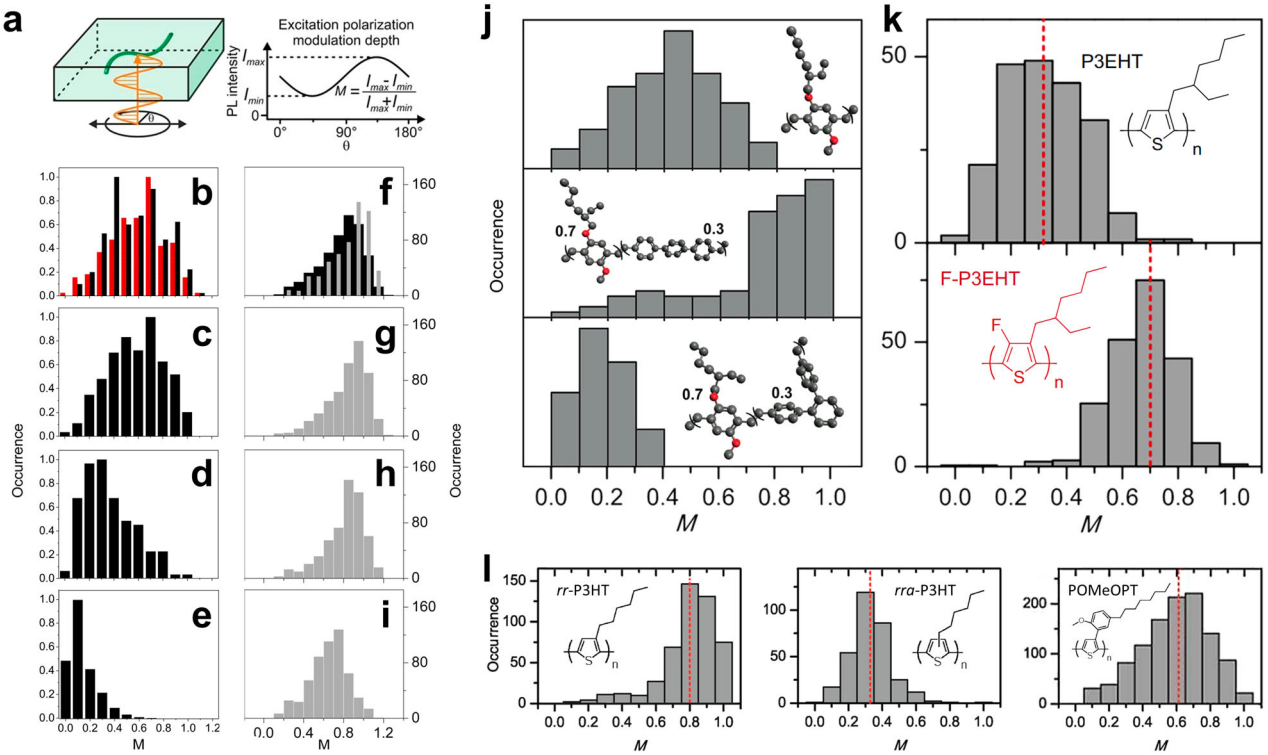

Fig. 5 Engineering of aggregate morphology. a Schematic illustration of the polarization modulation depth measurement technique and definition of modulation depth, *M*. Reproduced with permission from ref. [37]. Copyright 2015 National Academy of Sciences. **b**–**i** *M*-value histograms of single molecules and aggregates of MEH-PPV prepared using **b**–**e** chloroform and **f**–**i** toluene as the initial dissolving solvent. Histograms of the single-molecule *M* values before (red in **b** and black in **f**) and after (black in **b** and gray in **f**) SVA. The aggregates become larger from **c** to **d** to **e** and from **g** to **h** to **i**. The median *M* values are 0.66, 0.64, 0.63, 0.37, 0.16, 0.82, 0.91, 0.88, 0.85, and 0.67 for the red and black bars in **b**–**e** and black and gray bars in **f**–**i**, respectively. Reproduced with permission from ref. [76]. Copyright 2019 American Chemical Society. Reproduced with permission from ref. [77]. Copyright 2017 American Chemical Society. **j** *M*-value histograms of aggregates of pristine (top), 30% *para*-terphenyl (middle), and 30% *ortho*-terphenyl (bottom) MEH-PPV. The mean *M* values are 0.42, 0.76, and 0.18, respectively. Reproduced with permission from ref. [83]. Copyright 2011 American Chemical Society. **k** *M*-value histograms of aggregates of P3EHT (top) and F-P3EHT (bottom). The mean *M* values are 0.32 and 0.70, respectively. Reproduced with permission from ref. [84]. Copyright 2017 National Academy of Sciences. **l** *M*-value histograms of 100-chain *rr*-P3HT aggregates (left), 6-chain *rra*-P3HT aggregates (middle), and 4-chain POMeOPT aggregates (right). The mean *M* values are 0.80, 0.33, and 0.61, respectively. Reproduced with permission from ref. [93]. Copyright 2014 American Chemical Society.

comprising poly(3-hexylthiophene) (P3HT) with different regioregularity and side chain sizes: the CPs were regioregular P3HT (*rr*-P3HT), regiorandom P3HT (*rra*-P3HT), and poly(3-(2′-methoxy-5′-octylphenyl)thiophene) (POMeOPT)[93]. Notably, 100-chain *rr*-P3HT aggregates exhibited highly ordered interchain packing, whereas 6-chain *rra*-P3HT aggregates exhibited disordered packing, as reflected by mean *M* values of 0.80 and 0.33 for the former and the latter, respectively. This highlighted the crucial role that regioregularity plays in directing aggregate morphology. Moreover, POMeOPT aggregates consisted only of approximately 4 single chains and displayed a similar degree of morphological ordering as that of single chains with median $M \approx 0.61$ (Fig. 5l). POMeOPT exhibited poor efficiency in assembling into aggregates owing to the bulky side chains and side-chain-induced twisting of the backbone.

Distinct photophysics of CP aggregates compared with single-chain CPs

Single CP chains with ordered collapsed conformations often exhibit fluorescence intermittency, although they consist of numerous chromophores, indicating exciton funneling to a single, low-energy trap[94–106]. This finding from single-chain studies posed a question as to whether such robust exciton transfer can occur across length scales, surpassing the physical size of single CP chains. To address this, Yang et al. fabricated and investigated a series of CP aggregates with ordered anisotropic morphology[77]. As shown in Fig. 6a–h, MEH-PPV/PMMA blended films were prepared with different MEH-PPV concentrations. The SVA of these films with an acetone-chloroform solvent vapor mixture yielded MEH-PPV aggregates consisting of 40, 170, and 955 single chains on average. All aggregates exhibited

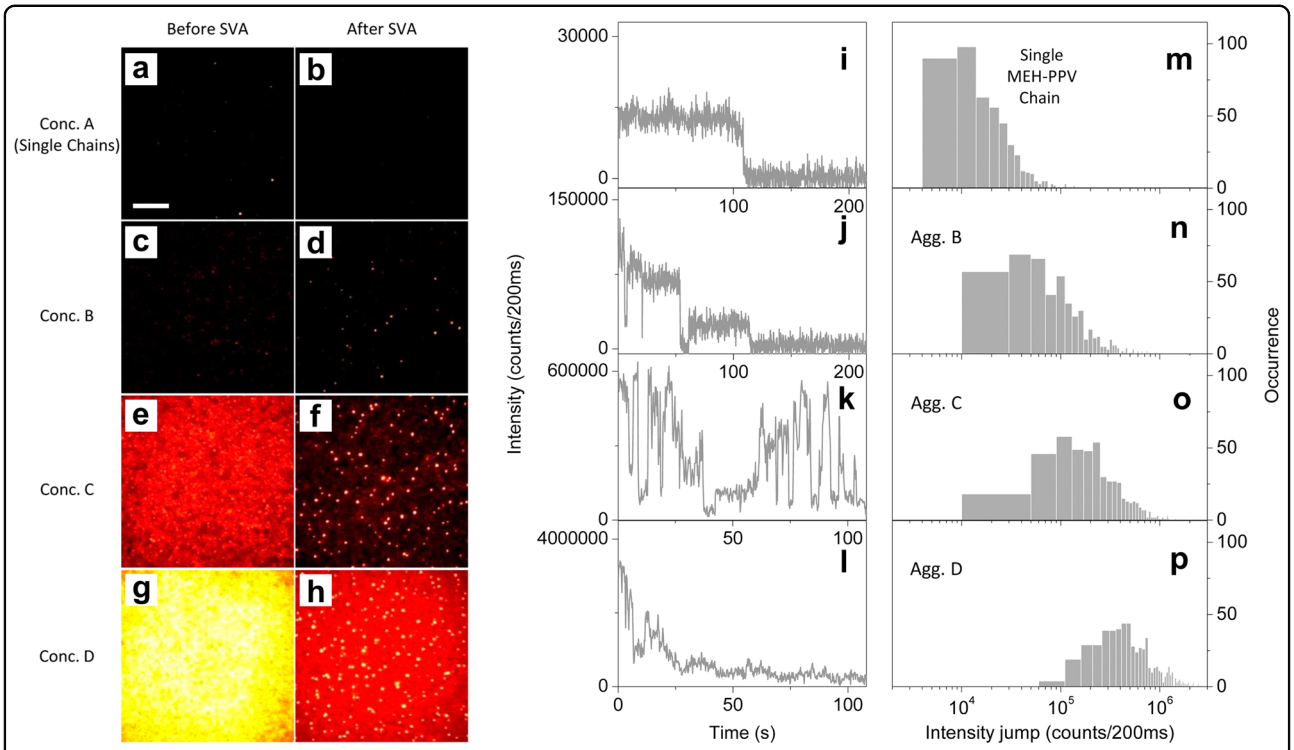

Fig. 6 Exciton transfer in highly ordered aggregates. a–h Wide-field fluorescence images of MEH-PPV/PMMA blended films of four different MEH-PPV concentrations **a**, **c**, **e**, **g** before and **b**, **d**, **f**, **h** after SVA. The concentrations were approximately 0.3, 3, 30, and 300 pM for A–D, respectively. **i–l** Typical fluorescence intensity trajectories and **m–p** histograms of jump size between adjacent fluorescence intensity levels for single MEH-PPV chains after SVA and aggregates B–D. Reproduced with permission from ref. [77]. Copyright 2017 American Chemical Society.

discrete changes in fluorescence intensity (Fig. 6i–l). Notably, the jump size between neighboring intensity levels was markedly greater in the aggregates than in the single chains and increased with the size of the aggregates (Fig. 6m–p), confirming efficient exciton diffusion at the mesoscopic length scale.

Triplet excitons are closely related to the efficiency of polymer solar cells because these species are long lived and detrimentally quench nearby singlet excitons via singlet–triplet annihilation. Steiner et al. explored the difference in triplet excitons between single-chain and mesoscopic multichain aggregates of P3HT[107]. The latter consisted of approximately 20 single chains. The authors compared the single-aggregate fluorescence intensity under nitrogen and air because molecular oxygen effectively quenches triplets[108]. Upon introducing air into a nitrogen environment, the intensity of the single-chain aggregates increased drastically, whereas that of the multichain aggregates was unchanged (Fig. 7a–d). Analysis of the intensity cross-correlation function $g^{(2)}(\Delta\tau)$ revealed an explicit exponential decay for the single-chain aggregates with a time constant of 18 μs, corresponding to the typical triplet lifetime of P3HT (Fig. 7e). In contrast, the multichain aggregates displayed a flat $g^{(2)}(\Delta\tau)$ curve (Fig. 7f), which led to the conclusion that no triplets were formed in them owing to mesoscale H-type interchain interactions[109].

Recently, Wilhelm et al. discovered the structural phase transition of CPs upon the formation of mesoscopic aggregates. Blue-emitting poly(9,9-dioctylfluorene) (PFO) can exist in three different structural phases depending on the intermonomer torsional angle Φ (Fig. 8a)[110]. In the α-phase, Φ is randomly distributed at approximately 135°, whereas in the β- and γ-phases, Φ lies in the range of 160–180° and 140–160°, respectively[111–113]. In fluorescence spectrum measurements, single PFO chains consistently exhibited a 0-0 peak at approximately 411 nm, characteristic of the α-phase (Fig. 8b). Owing to the randomness of Φ in this phase, each chain exhibited a different degree of bending in the backbone, as is evident from the distribution of the 0-1/0-0 peak ratio. Compared with these single α-phase PFO chains, mesoscopic aggregates consisting of approximately 34 single chains exhibited a marked redshift of the 0-0 peak, which correlated with a decrease in the 0-1/0-0 peak ratio (Fig. 8c). This revealed that aggregation induces a phase transition to more ordered β- and γ-phases with enhanced intrachain coupling. Similar changes in the intrachain morphology of CPs induced by aggregation have been reported in other studies[76,77].

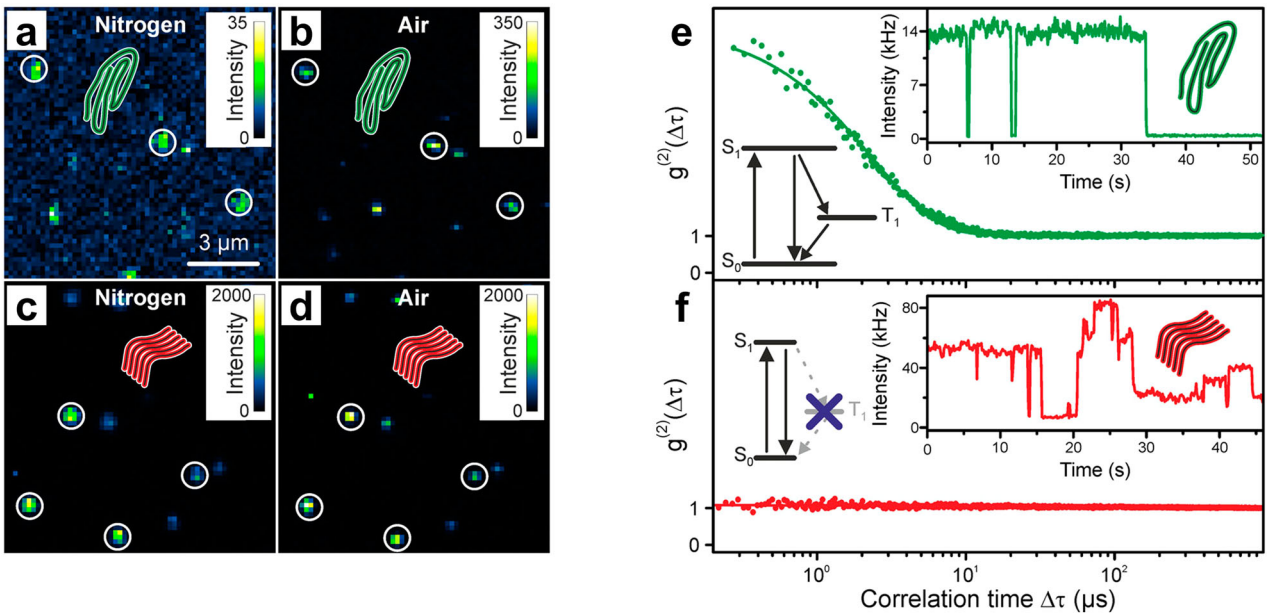

Fig. 7 Triplet excitons in multichain aggregates. a–**d** Fluorescence images of **a**, **b** single-chain and **c**, **d** multichain P3HT aggregates measured in either nitrogen or air. **e**, **f** Intensity cross-correlation function $g^{(2)}(\Delta\tau)$ obtained from averaging data of **e** 50 single-chain aggregates and **f** 150 multichain aggregates under a nitrogen atmosphere. The insets show typical fluorescence intensity trajectories from which $g^{(2)}(\Delta\tau)$ was calculated. Reproduced with permission from ref. [107]. Copyright 2017 American Chemical Society.

Beyond prototypical CP experiments

While SVA studies of single chains and aggregates have focused primarily on prototypical CPs such as MEH-PPV, P3HT, PFO, and their derivatives, the SVA technique is now more widely applied to study the relationship between the conformation and photophysics of conjugated materials at the single-molecule level[114–119]. Specifically, SVA of background matrix films containing single molecules of interest at very low concentrations using vapors of a single solvent allows the molecules of interest to undergo conformational dynamics. This allows the direct comparison of structural and photophysical properties before and after SVA for a variety of single molecules.

Kim et al. directly visualized SVA-induced conformational changes in individual porphyrin-based polymers (*Zn*, $n = 3$, 4, 5, 6, 8, 12, 24, 32, 48, 64, 96, and 128)[120]. They utilized super-resolution localization microscopy, in which a series of emission centroid positions of a single *Zn* molecule determined as a function of consecutive photobleaching and photoblinking events allowed the determination of polymer conformation at the nanometer length scale. A typical example is that of a single Z96 molecule embedded in a PMMA film; the distribution of its emission centroid positions was initially constrained to a very small region. However, it became significantly elongated after SVA (Fig. 9), demonstrating the conformational transition of the molecule from a coiled to a more stretched conformation.

In addition to polymer conformation, Vogelsang et al. showed that the position and orientation of individual macrocyclic oligomers in PMMA films could be manipulated via SVA[121]. Following SVA, the macrocycles accumulated preferentially at the PMMA/air interface, as indicated by the disappearance of the single-molecule intensity cross-correlation signal. This was due to triplet state quenching by molecular oxygen, which was more accessible at the interface than deep within the film (Fig. 10b). Furthermore, the macrocycles primarily adopted an orientation parallel to the substrate surface at the interface. This was evidenced by the fact that the *M* value distribution peaked at approximately 0.1 (Fig. 10c). Owing to ring symmetry, macrocycles lying parallel to the surface exhibited isotropic absorption and yielded *M* values near 0.

In conventional single-molecule approaches, the conformational dynamics of individual CPs are unavoidably constrained in solvent-swollen host matrices and semi-liquid media, such as liquid crystals and viscous solutions. To circumvent interference from the surrounding environment, Penedo et al. introduced glass surface anchoring of polymer chains via triethoxysilane (TES) functionalization of one end of the polymer (Fig. 11a)[122]. This approach impedes polymer diffusion in organic solvent environments while ensuring conformational flexibility. Single surface-anchored P3HT chains in good (*o*-dichlorobenzene, *o*-DCB) and poor (DMSO) solvents

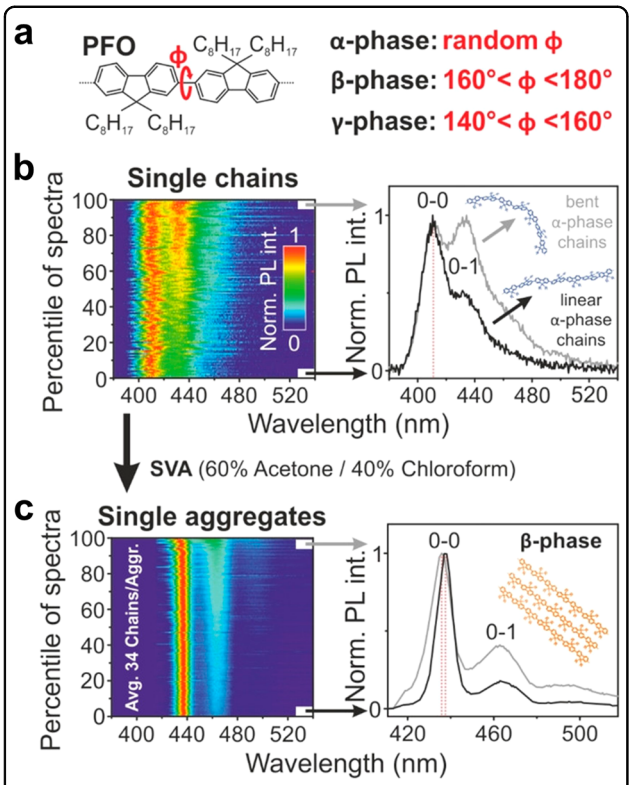

Fig. 8 Structural phase transition upon aggregation. a Structure of PFO and its three different structural phases (α-, β-, and γ-phases) depending on the fluorene–fluorene torsional angle Φ. **b**, **c** Shown at left are the normalized fluorescence spectra of **b** 24 single PFO chains and **c** 173 PFO aggregates sorted according to their 0-1/0-0 peak ratio. Shown at right are the summed spectra for 5% subpopulations with high (gray) and low (black) peak ratios. Reproduced with permission from ref. [110]. Copyright 2020 John Wiley and Sons.

displayed chain-to-chain conformational heterogeneity, as indicated by the diversity of the single-molecule fluorescence intensity profiles (Fig. 11b). Real-time solvent exchange experiments showed that single surface-anchored P3HT chains dynamically reorganize their conformation on a subsecond time scale in response to sudden changes in solvent quality (Fig. 11c, d).

Conclusions

This review has provided an overview of single-aggregate spectroscopic studies on CP aggregates. The SVA technique offers a unique opportunity for the bottom-up preparation and structural characterization and control of mesoscopic aggregates of CPs. These entities, compared to single CPs, provide environments more analogous to those present in thin-film devices in terms of complexity of morphology and chain interactions; thus, such aggregates hold the potential to provide information that is more relevant to optoelectronic device function. From a technical perspective, SVA for the formation of CP aggregates in swollen films requires the following two conditions to be satisfied: (1) the CP concentration must be at least an order of magnitude higher than that typical of single-chain studies, and (2) a good–poor-solvent mixture with an appropriate vapor volume ratio must be used. These conditions arise from the prediction that CP aggregate formation and growth rely on Ostwald ripening. This is partially true, but aggregate growth is more complex and occurs through multiple mechanisms: Ostwald ripening, as predicted, and aggregate coalescence. One study showed that these two mechanisms contribute to aggregate growth to similar extents; however, they have a distinctive impact on aggregate morphology, particularly in terms of the

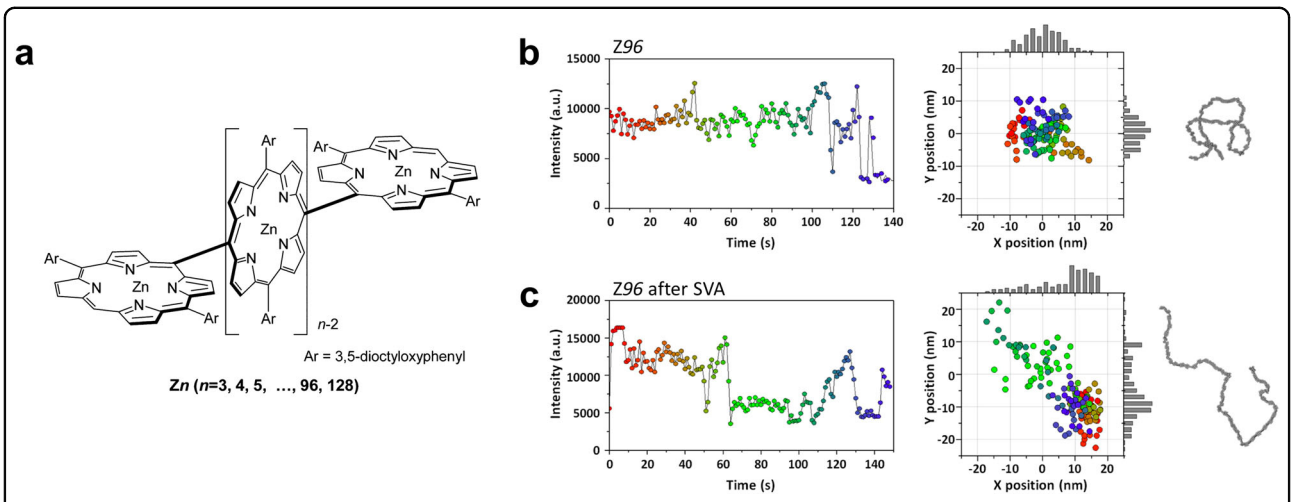

Fig. 9 SVA-induced conformational changes in porphyrin-based polymers. a Molecular structure of *meso–meso* directly linked porphyrin arrays (*Zn*). **b**, **c** Color-coded fluorescence intensity trajectories (left) and emission centroid positions (middle) of a single Z96 molecule **b** before and **c** after SVA. Shown at right are illustrative molecular conformations corresponding to the distributions of the centroid positions. Reproduced with permission from ref. [120]. Copyright 2018 American Chemical Society.

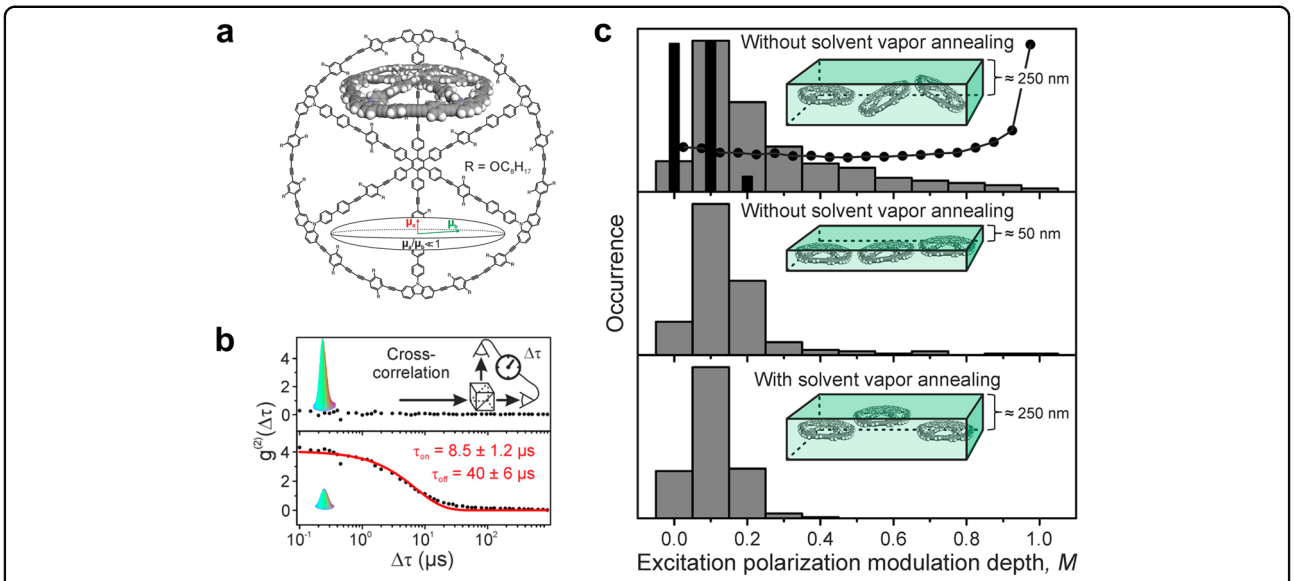

Fig. 10 Rearrangement of macrocyclic oligomers in a polymer film by SVA. a Molecular structure of a shape-persistent spoked-wheel molecule. **b** $g^{(2)}(\Delta\tau)$ curves for 39 and 254 macrocycles exhibiting high and low single-molecule fluorescence intensities. **c** *M*-value histograms of macrocycles dispersed in a 250 nm-thick PMMA film without (top) and with (bottom) SVA and in a 50 nm-thick PMMA film without SVA (middle). The black dots represent a simulated *M* distribution for macrocycles with random orientations in three dimensions. The black bars represent the instrument response measured using isotropic fluorescent beads. Reproduced with permission from ref. [121]. Copyright 2016 American Chemical Society.

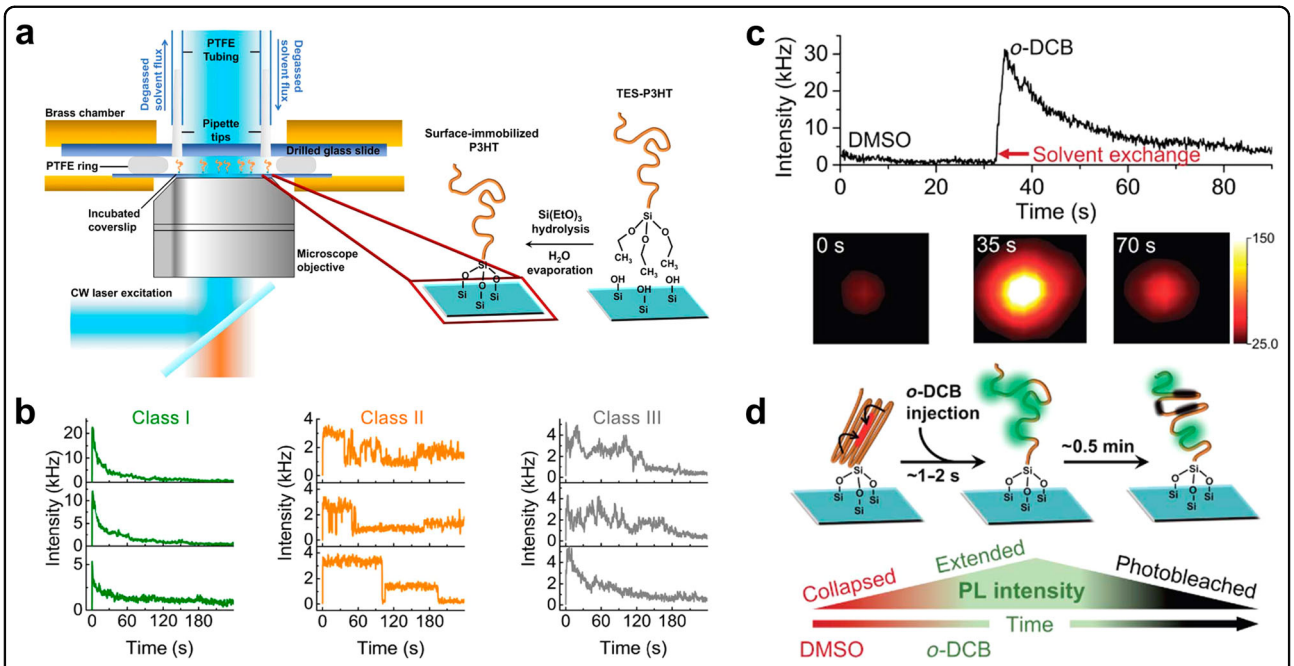

Fig. 11 Conformation dynamics of CPs in organic solvents. a Schematic of the strategy for studying single P3HT chains in 100% organic solvents. **b** Three different classes of fluorescence intensity trajectories of surface-anchored TES-P3HT-L chains. **c** Fluorescence intensity trajectory of a single TES-P3HT-S chain showing a sudden change in intensity upon switching from the poor solvent (DMSO) to the good solvent (*o*-DCB) at ~31 s and corresponding fluorescence images taken at $t = 0$, 35, and 70 s. **d** Schematic illustrating the collapsed-to-extended conformational change that occurred during the in situ solvent-exchange experiment shown in **c**. Reproduced with permission from ref. [122]. Copyright 2018 American Association for the Advancement of Science.

degree of mesoscopic order. The morphological order of CP aggregates plays a key role in determining the type and extent of electronic coupling and photophysics: intrachain and interchain ordering lead to J- and H-type coupling, respectively, causing the aggregates to exhibit the associated spectroscopic and photophysical properties. Clearly, an ordered morphology ensures robust chain interactions, which are crucial for achieving long-range exciton diffusion, which is required for bulk heterojunction solar cell applications. In most cases, the degree of order in the aggregate morphology is already templated at the single-molecule level; that is, highly ordered anisotropic aggregates are formed primarily by the assembly of single CPs with collapsed, ordered conformations. As such, a multitude of studies have been devoted to tailoring the chain backbone and side chains to attain order over single CPs and, in turn, aggregates thereof. These studies have collectively shown that ordered CP aggregates exhibit designed properties such as enlarged exciton domains and exciton transfers over tens of nanometers.

In summary, this review and the literature referred to herein shed light on the mesoscopic connections between morphology, chain interactions, and photophysics in CPs. This understanding, in conjunction with that established at the single-molecule level, will facilitate the bottom-up control of optoelectronic properties from the molecular to the device-length scale.

Acknowledgements
J.Y. and K.P. acknowledge support from National Research Foundation of Korea (NRF) grants funded by the Korean government (MSIT) (2021R1F1A1050428 and 2022R1A4A1032832). L.J.K. acknowledges support from the National Science Foundation (CHE 1807931).

Author details
[1]Department of Chemistry, Yonsei University, Wonju, Gangwon 26493, Korea. [2]Department of Chemistry, Columbia University, New York, NY 10027, USA. [3]Department of Chemistry, Sungkyunkwan University, Suwon 16419, Korea

Author contributions
J.Y., L.J.K., and K.P. conceived the theme and directed the project. C.K. and J.Y. collected the literature and wrote the manuscript. C.K. and H.J. prepared the figures. L.J.K. and H.J.K. reviewed and edited the manuscript. All authors read and approved the final manuscript.

Conflict of interest
The authors declare no competing interests.

Received: 10 January 2023 Revised: 6 April 2023 Accepted: 14 April 2023.
Published online: 19 May 2023

References

1. Coakley, K. M. & McGehee, M. D. Conjugated polymer photovoltaic cells. *Chem. Mater.* **16**, 4533–4542 (2004).
2. Friend, R. H. et al. Electroluminescence in conjugated polymers. *Nature* **397**, 121–128 (1999).
3. Günes, S., Neugebauer, H. & Sariciftci, N. S. Conjugated polymer-based organic solar cells. *Chem. Rev.* **107**, 1324–1338 (2007).
4. Facchetti, A. π-Conjugated polymers for organic electronics and photovoltaic cell applications. *Chem. Mater.* **23**, 733–758 (2011).
5. Lu, L. & Yu, L. Understanding low bandgap polymer PTB7 and optimizing polymer solar cells based on it. *Adv. Mater.* **26**, 4413–4430 (2014).
6. Zheng, H. et al. All-solution processed polymer light-emitting diode displays. *Nat. Commun.* **4**, 1971 (2013).
7. McQuade, D. T., Pullen, A. E. & Swager, T. M. Conjugated polymer-based chemical sensors. *Chem. Rev.* **100**, 2537–2574 (2000).
8. Yang, J., Zhao, Z., Wang, S., Guo, Y. & Liu, Y. Insight into high-performance conjugated polymers for organic field-effect transistors. *Chem.* **4**, 2748–2785 (2018).
9. Scheblykin, I. G., Yartsev, A., Pullerits, T., Gulbinas, V. & Sundström, V. Excited state and charge photogeneration dynamics in conjugated polymers. *J. Phys. Chem. B* **111**, 6303–6321 (2007).
10. Barbara, P. F., Gesquiere, A. J., Park, S.-J. & Lee, Y. J. Single-molecule spectroscopy of conjugated polymers. *Acc. Chem. Res.* **38**, 602–610 (2005).
11. Bronstein, H., Nielsen, C. B., Schroeder, B. C. & McCulloch, I. The role of chemical design in the performance of organic semiconductors. *Nat. Rev. Chem.* **4**, 66–77 (2020).
12. Zhao, F., Wang, C. & Zhan, X. Morphology control in organic solar cells. *Adv. Energy Mater.* **8**, 1703147 (2018).
13. Kaake, L. G., Barbara, P. F. & Zhu, X. Y. Intrinsic charge trapping in organic and polymeric semiconductors: a physical chemistry perspective. *J. Phys. Chem. Lett.* **1**, 628–635 (2010).
14. Liang, Y. & Yu, L. A new class of semiconducting polymers for bulk heterojunction solar cells with exceptionally high performance. *Acc. Chem. Res.* **43**, 1227–1236 (2010).
15. Meredith, P., Bettinger, C. J., Irimia-Vladu, M., Mostert, A. B. & Schwenn, P. E. Electronic and optoelectronic materials and devices inspired by nature. *Rep. Prog. Phys.* **76**, 034501 (2013).
16. van Franeker, J. J. et al. Polymer solar cells: Solubility controls fiber network formation. *J. Am. Chem. Soc.* **137**, 11783–11794 (2015).
17. Wang, D. et al. New insights into morphology of high performance BHJ photovoltaics revealed by high resolution AFM. *Nano Lett.* **14**, 5727–5732 (2014).
18. Li, W. et al. Effect of the fibrillar microstructure on the efficiency of high molecular weight diketopyrrolopyrrole-based polymer solar cells. *Adv. Mater.* **26**, 1565–1570 (2014).
19. Levin, A. et al. Ostwald's rule of stages governs structural transitions and morphology of dipeptide supramolecular polymers. *Nat. Commun.* **5**, 5219 (2014).
20. Noriega, R. et al. A general relationship between disorder, aggregation and charge transport in conjugated polymers. *Nat. Mater.* **12**, 1038–1044 (2013).
21. Hedley, G. J. et al. Determining the optimum morphology in high-performance polymer-fullerene organic photovoltaic cells. *Nat. Commun.* **4**, 2867 (2013).
22. Ostrowski, D. P. et al. The effects of aggregation on electronic and optical properties of oligothiophene particles. *ACS Nano* **6**, 5507–5513 (2012).
23. Jung, J. W., Liu, F., Russell, T. P. & Jo, W. H. A high mobility conjugated polymer based on dithienothiophene and diketopyrrolopyrrole for organic photovoltaics. *Energy Environ. Sci.* **5**, 6857–6861 (2012).
24. Österbacka, R., An, C. P., Jiang, X. M. & Vardeny, Z. V. Two-dimensional electronic excitations in self-assembled conjugated polymer nanocrystals. *Science* **287**, 839–842 (2000).
25. Sahoo, D., Tian, Y., Sforazzini, G., Anderson, H. L. & Scheblykin, I. G. Photo-induced fluorescence quenching in conjugated polymers dispersed in solid matrices at low concentration. *J. Mater. Chem. C* **2**, 6601–6608 (2014).
26. Hou, L., Adhikari, S., Tian, Y., Scheblykin, I. G. & Orrit, M. Absorption and quantum yield of single conjugated polymer poly[2-methoxy-5-(2-ethylhexyloxy)-1,4-phenylenevinylene] (MEH-PPV) molecules. *Nano Lett.* **17**, 1575–1581 (2017).
27. Hestand, N. J. & Spano, F. C. Molecular aggregate photophysics beyond the Kasha model: novel design principles for organic materials. *Acc. Chem. Res.* **50**, 341–350 (2017).
28. Li, S. et al. Influence of covalent and noncovalent backbone rigidification strategies on the aggregation structures of a wide-band-gap polymer for photovoltaic cells. *Chem. Mater.* **32**, 1993–2003 (2020).

29. Nguyen, T.-Q., Kwong, R. C., Thompson, M. E. & Schwartz, B. J. Improving the performance of conjugated polymer-based devices by control of interchain interactions and polymer film morphology. *Appl. Phys. Lett.* **76**, 2454–2456 (2000).
30. Nguyen, T.-Q., Martini, I. B., Liu, J. & Schwartz, B. J. Controlling interchain interactions in conjugated polymers: the effects of chain morphology on exciton–exciton annihilation and aggregation in MEH—PPV films. *J. Phys. Chem. B* **104**, 237–255 (2000).
31. Schwartz, B. J. Conjugated polymers as molecular materials: how chain conformation and film morphology influence energy transfer and interchain interactions. *Annu. Rev. Phys. Chem.* **54**, 141–172 (2003).
32. Hu, Z., Shao, B., Geberth, G. T. & Vanden Bout, D. A. Effects of molecular architecture on morphology and photophysics in conjugated polymers: from single molecules to bulk. *Chem. Sci.* **9**, 1101–1111 (2018).
33. Wang, H. et al. Structure and morphology control in thin films of conjugated polymers for an improved charge transport. *Polymers* **5**, 1272–1324 (2013).
34. Thiessen, A. et al. Unraveling the chromophoric disorder of poly(3-hexylthiophene). *Proc. Natl Acad. Sci. USA* **110**, E3550–E3556 (2013).
35. Riera-Galindo, S., Tamayo, A. & Mas-Torrent, M. Role of polymorphism and thin-film morphology in organic semiconductors processed by solution shearing. *ACS Omega* **3**, 2329–2339 (2018).
36. Gao, X. et al. Morphology and transport characterization of solution-processed rubrene thin films on polymer-modified substrates. *Sci. Rep.* **10**, 12183 (2020).
37. Stangl, T. et al. Mesoscopic quantum emitters from deterministic aggregates of conjugated polymers. *Proc. Natl Acad. Sci. USA* **112**, E5560–E5566 (2015).
38. Zhu, X. et al. Unidirectional and crystalline organic semiconductor microwire arrays by solvent vapor annealing with PMMA as the assisting layer. *J. Mater. Chem. C* **6**, 12479–12483 (2018).
39. Marques, S. R.-M., Selhorst, R. C., Venkataraman, D. & Barnes, M. D. Probing the evolution of molecular packing underlying HJ-aggregate transition in organic semiconductors using solvent vapor annealing. *J. Phys. Chem. C* **123**, 28948–28957 (2019).
40. Schulz, G. L. & Ludwigs, S. Controlled crystallization of conjugated polymer films from solution and solvent vapor for polymer electronics. *Adv. Funct. Mater.* **27**, 1603083 (2017).
41. Chen, H., Hsiao, Y.-C., Hu, B. & Dadmun, M. Tuning the morphology and performance of low bandgap polymer: fullerene heterojunctions via solvent annealing in selective solvents. *Adv. Funct. Mater.* **24**, 5129–5136 (2014).
42. Jo, G., Jung, J. & Chang, M. Controlled self-assembly of conjugated polymers via a solvent vapor pre-treatment for use in organic field-effect transistors. *Polymers* **11**, 332 (2019).
43. Shi, J. et al. Photo-oxidation reveals H-aggregates hidden in spin-cast-conjugated polymer films as observed by two-dimensional polarization imaging. *Chem. Mater.* **31**, 8927–8936 (2019).
44. Trefz, D. et al. Tuning orientational order of highly aggregating p(NDI2OD-T_2) by solvent vapor annealing and blade coating. *Macromolecules* **52**, 43–54 (2019).
45. Vogelsang, J., Adachi, T., Brazard, J., Vanden Bout, D. A. & Barbara, P. F. Self-assembly of highly ordered conjugated polymer aggregates with long-range energy transfer. *Nat. Mater.* **10**, 942–946 (2011).
46. Lindvig, T., Michelsen, M. L. & Kontogeorgis, G. M. A Flory–Huggins model based on the Hansen solubility parameters. *Fluid Phase Equilib.* **203**, 247–260 (2002).
47. Hoang, D. T. et al. In situ multi-modal monitoring of solvent vapor swelling in polymer thin films. *Rev. Sci. Instrum.* **87**, 015106 (2016).
48. Voorhees, P. W. The theory of Ostwald ripening. *J. Stat. Phys.* **38**, 231–252 (1985).
49. Baldan, A. Review progress in Ostwald ripening theories and their applications to nickel-base superalloys. Part I: Ostwald ripening theories. *J. Mater. Sci.* **37**, 2171–2202 (2002).
50. Yao, J. H., Elder, K. R., Guo, H. & Grant, M. Theory and simulation of Ostwald ripening. *Phys. Rev. B* **47**, 14110–14125 (1993).
51. Yec, C. C. & Zeng, H. C. Synthesis of complex nanomaterials via Ostwald ripening. *J. Mater. Chem. A* **2**, 4843–4851 (2014).
52. Vogelsang, J. & Lupton, J. M. Solvent vapor annealing of single conjugated polymer chains: building organic optoelectronic materials from the bottom up. *J. Phys. Chem. Lett.* **3**, 1503–1513 (2012).
53. Yang, J., Park, H. & Kaufman, L. J. In situ optical imaging of the growth of conjugated polymer aggregates. *Angew. Chem. Int. Ed.* **57**, 1826–1830 (2018).
54. Martin, T. P. et al. Packing dependent electronic coupling in single poly(3-hexylthiophene) H- and J-aggregate nanofibers. *J. Phys. Chem. B* **117**, 4478–4487 (2013).
55. Deng, Y., Yuan, W., Jia, Z. & Liu, G. H- and J-aggregation of fluorene-based chromophores. *J. Phys. Chem. B* **118**, 14536–14545 (2014).
56. Más-Montoya, M. & Janssen, R. A. J. The effect of H- and J-aggregation on the photophysical and photovoltaic properties of small thiophene–pyridine–DPP molecules for bulk-heterojunction solar cells. *Adv. Funct. Mater.* **27**, 1605779 (2017).
57. Eder, T. et al. Interplay between J- and H-type coupling in aggregates of π-conjugated polymers: a single-molecule perspective. *Angew. Chem. Int. Ed.* **58**, 18898–18902 (2019).
58. Ziffer, M. E. et al. Tuning H- and J-aggregate behavior in π-conjugated polymers via noncovalent interactions. *J. Phys. Chem. C* **122**, 18860–18869 (2018).
59. Liess, A. et al. Exciton coupling of merocyanine dyes from H- to J-type in the solid state by crystal engineering. *Nano Lett.* **17**, 1719–1726 (2017).
60. Chen, L. et al. Tuning the π-π stacking distance and J-aggregation of DPP-based conjugated polymer via introducing insulating polymer. *J. Polym. Sci. B Polym. Phys.* **54**, 838–847 (2016).
61. Siddiqui, S. & Spano, F. C. H- and J-aggregates of conjugated polymers and oligomers: a theoretical investigation. *Chem. Phys. Lett.* **308**, 99–105 (1999).
62. Spano, F. C. The spectral signatures of Frenkel polarons in H- and J-aggregates. *Acc. Chem. Res.* **43**, 429–439 (2010).
63. Niles, E. T. et al. J-aggregate behavior in poly-3-hexylthiophene nanofibers. *J. Phys. Chem. Lett.* **3**, 259–263 (2012).
64. Spano, F. C. & Silva, C. H- and J-aggregate behavior in polymeric semiconductors. *Annu. Rev. Phys. Chem.* **65**, 477–500 (2014).
65. Hestand, N. J. & Spano, F. C. Expanded theory of H- and J-molecular aggregates: the effects of vibronic coupling and intermolecular charge transfer. *Chem. Rev.* **118**, 7069–7163 (2018).
66. Hestand, N. J. & Spano, F. C. Interference between Coulombic and CT-mediated couplings in molecular aggregates: H- to J-aggregate transformation in perylene-based π-stacks. *J. Chem. Phys.* **143**, 244707 (2015).
67. Yamagata, H. & Spano, F. C. Strong photophysical similarities between conjugated polymers and J-aggregates. *J. Phys. Chem. Lett.* **5**, 622–632 (2014).
68. Yamagata, H. et al. The red-phase of poly[2-methoxy-5-(2-ethylhexyloxy)-1,4-phenylenevinylene] (MEH-PPV): a disordered HJ-aggregate. *J. Chem. Phys.* **139**, 114903 (2013).
69. Eder, T. et al. Switching between H- and J-type electronic coupling in single conjugated polymer aggregates. *Nat. Commun.* **8**, 1641 (2017).
70. Hu, D. et al. Collapse of stiff conjugated polymers with chemical defects into ordered, cylindrical conformations. *Nature* **405**, 1030–1033 (2000).
71. Nguyen, T.-Q., Doan, V. & Schwartz, B. J. Conjugated polymer aggregates in solution: control of interchain interactions. *J. Chem. Phys.* **110**, 4068–4078 (1999).
72. Traiphol, R. et al. Effects of chain conformation and chain length on degree of aggregation in assembled particles of conjugated polymer in solvents–nonsolvent: a spectroscopic study. *J. Polym. Sci. B Polym. Phys.* **48**, 894–904 (2010).
73. Li, T. et al. Effect of solvent on the solution state of conjugated polymer P7DPF including single-chain to aggregated state structure formation, dynamic evolution, and related mechanisms. *Macromolecules* **53**, 4264–4273 (2020).
74. Zhang, H. et al. Effect of solvents on the solution state and film condensed state structures of a polyfluorene conjugated polymer in the dynamic evolution process from solution to film. *J. Phys. Chem. C* **123**, 27317–27326 (2019).
75. Xu, Z., Tsai, H., Wang, H.-L. & Cotlet, M. Solvent polarity effect on chain conformation, film morphology, and optical properties of a water-soluble conjugated polymer. *J. Phys. Chem. B* **114**, 11746–11752 (2010).
76. Kwon, Y. & Kaufman, L. J. Nearly isotropic conjugated polymer aggregates with efficient local exciton diffusion. *J. Phys. Chem. C* **123**, 29418–29426 (2019).
77. Yang, J., Park, H. & Kaufman, L. J. Highly anisotropic conjugated polymer aggregates: preparation and quantification of physical and optical anisotropy. *J. Phys. Chem. C* **121**, 13854–13862 (2017).
78. Jackson, N. E. et al. Conformational order in aggregates of conjugated polymers. *J. Am. Chem. Soc.* **137**, 6254–6262 (2015).
79. Blatchford, J. W. et al. Photoluminescence in pyridine-based polymers: role of aggregates. *Phys. Rev. B* **54**, 9180–9189 (1996).

80. Peteanu, L. A. et al. Visualizing core–shell structure in substituted PPV oligomer aggregates using fluorescence lifetime imaging microscopy (FLIM). *J. Phys. Chem. C* **115**, 15607–15616 (2011).
81. Peteanu, L. A., Chowdhury, S., Wildeman, J. & Sfeir, M. Y. Exciton–exciton annihilation as a probe of interchain interactions in PPV–oligomer aggregates. *J. Phys. Chem. B* **121**, 1707–1714 (2017).
82. O'Carroll, D. M. et al. Conjugated polymer-based photonic nanostructures. *Polym. Chem.* **4**, 5181–5196 (2013).
83. Traub, M. C. et al. Unmasking bulk exciton traps and interchain electronic interactions with single conjugated polymer aggregates. *ACS Nano* **6**, 523–529 (2012).
84. Hu, Z. et al. Impact of backbone fluorination on nanoscale morphology and excitonic coupling in polythiophenes. *Proc. Natl Acad. Sci. USA* **114**, 5113–5118 (2017).
85. Raithel, D. et al. Direct observation of backbone planarization via side-chain alignment in single bulky-substituted polythiophenes. *Proc. Natl Acad. Sci. USA* **115**, 2699–2704 (2018).
86. Carbonnier, B., Egbe, D. A. M., Birckner, E., Grummt, U.-W. & Pakula, T. Correlation between chain packing and photoluminescence for PPV/PPE in macroscopically oriented state: side chain effects. *Macromolecules* **38**, 7546–7554 (2005).
87. Wedler, S. et al. What is the role of planarity and torsional freedom for aggregation in a π-conjugated donor–acceptor model oligomer? *J. Mater. Chem. C* **8**, 4944–4955 (2020).
88. Fei, Z. et al. Influence of backbone fluorination in regioregular poly(3-alkyl-4-fluoro)thiophenes. *J. Am. Chem. Soc.* **137**, 6866–6879 (2015).
89. He, G. et al. A new strategy for designing conjugated polymer-based fluorescence sensing films via introduction of conformation controllable side chains. *Macromolecules* **44**, 703–710 (2011).
90. Sahoo, D., Sugiyasu, K., Tian, Y., Takeuchi, M. & Scheblykin, I. G. Effect of conjugated backbone protection on intrinsic and light-induced fluorescence quenching in polythiophenes. *Chem. Mater.* **26**, 4867–4875 (2014).
91. Clark, J., Silva, C., Friend, R. H. & Spano, F. C. Role of intermolecular coupling in the photophysics of disordered organic semiconductors: aggregate emission in regioregular polythiophene. *Phys. Rev. Lett.* **98**, 206406 (2007).
92. Chen, M. S. et al. Control of polymer-packing rrientation in thin films through synthetic tailoring of backbone coplanarity. *Chem. Mater.* **25**, 4088–4096 (2013).
93. Hu, Z. et al. Excitonic energy migration in conjugated polymers: The critical role of interchain morphology. *J. Am. Chem. Soc.* **136**, 16023–16031 (2014).
94. Huser, T., Yan, M. & Rothberg, L. J. Single chain spectroscopy of conformational dependence of conjugated polymer photophysics. *Proc. Natl Acad. Sci. USA* **97**, 11187–11191 (2000).
95. Steiner, F., Vogelsang, J. & Lupton, J. M. Singlet-triplet annihilation limits exciton yield in poly(3-Hexylthiophene). *Phys. Rev. Lett.* **112**, 137402 (2014).
96. Park, H., Hoang, D. T., Paeng, K., Yang, J. & Kaufman, L. J. Conformation-dependent photostability among and within single conjugated polymers. *Nano Lett.* **15**, 7604–7609 (2015).
97. Brown, P. J. et al. Effect of interchain interactions on the absorption and emission of poly(3-hexylthiophene). *Phys. Rev. B* **67**, 064203 (2003).
98. Lin, H. et al. Fluorescence blinking, exciton dynamics, and energy transfer domains in single conjugated polymer chains. *J. Am. Chem. Soc.* **130**, 7042–7051 (2008).
99. Habuchi, S., Onda, S. & Vacha, M. Molecular weight dependence of emission intensity and emitting sites distribution within single conjugated polymer molecules. *Phys. Chem. Chem. Phys.* **13**, 1743–1753 (2011).
100. Adachi, T. et al. Conformational effect on energy transfer in single polythiophene chains. *J. Phys. Chem. B* **116**, 9866–9872 (2012).
101. Traub, M. C., Lakhwani, G., Bolinger, J. C., Bout, D. V. & Barbara, P. F. Electronic energy transfer in highly aligned MEH-PPV single chains. *J. Phys. Chem. B* **115**, 9941–9947 (2011).
102. Park, H., Kwon, Y. & Kaufman, L. J. Complex photophysical behaviors affect single conjugated molecule optical anisotropy measurements. *J. Phys. Chem. C* **123**, 1960–1965 (2019).
103. Lupton, J. M. Chromophores in conjugated polymers—all straight? *ChemPhysChem* **13**, 901–907 (2012).
104. Li, Y.-C. et al. Scattering study of the conformational structure and aggregation behavior of a conjugated polymer solution. *Langmuir* **25**, 4668–4677 (2009).
105. Pullerits, T., Mirzov, O. & Scheblykin, I. G. Conformational fluctuations and large fluorescence spectral diffusion in conjugated polymer single chains at low temperatures. *J. Phys. Chem. B* **109**, 19099–19107 (2005).
106. Lin, H. et al. Fate of excitations in conjugated polymers: single-molecule spectroscopy reveals nonemissive "dark" regions in MEH-PPV individual chains. *Nano Lett.* **9**, 4456–4461 (2009).
107. Steiner, F., Lupton, J. M. & Vogelsang, J. Role of triplet-state shelving in organic photovoltaics: single-chain aggregates of poly(3-hexylthiophene) versus mesoscopic multichain aggregates. *J. Am. Chem. Soc.* **139**, 9787–9790 (2017).
108. Grewer, C. & Brauer, H.-D. Mechanism of the triplet-state quenching by molecular oxygen in solution. *J. Phys. Chem.* **98**, 4230–4235 (1994).
109. Thomas, A. K., Garcia, J. A., Ulibarri-Sanchez, J., Gao, J. & Grey, J. K. High intrachain order promotes triplet formation from recombination of long-lived polarons in poly(3-hexylthiophene) J-aggregate nanofibers. *ACS Nano* **8**, 10559–10568 (2014).
110. Wilhelm, P., Blank, D., Lupton, J. M. & Vogelsang, J. Control of intrachain morphology in the formation of polyfluorene aggregates on the single-molecule level. *ChemPhysChem* **21**, 961–965 (2020).
111. Chunwaschirasiri, W., Tanto, B., Huber, D. L. & Winokur, M. J. Chain conformations and photoluminescence of poly(di-n-octylfluorene). *Phys. Rev. Lett.* **94**, 107402 (2005).
112. Grell, M. et al. Chain geometry, solution aggregation and enhanced dichroism in the liquidcrystalline conjugated polymer poly(9,9-dioctylfluorene). *Acta Polym.* **49**, 439–444 (1998).
113. Tsoi, W. C. & Lidzey, D. G. Raman spectroscopy of fluorene oligomers in the α-, β- and γ-phases. *J. Phys. Condens. Matter* **20**, 125213 (2008).
114. Vogelsang, J., Brazard, J., Adachi, T., Bolinger, J. C. & Barbara, P. F. Watching the annealing process one polymer chain at a time. *Angew. Chem. Int. Ed.* **50**, 2257–2261 (2011).
115. Fu, Y. & Lakowicz, J. R. A closer look at polymer annealing. *Nature* **472**, 178–179 (2011).
116. Wise, A. J. & Grey, J. K. Understanding the structural evolution of single conjugated polymer chain conformers. *Polymers* **8**, 388 (2016).
117. Wang, H. et al. In situ observation of organic single micro-crystal fabrication by solvent vapor annealing. *J. Mater. Chem. C* **9**, 9124–9129 (2021).
118. Bolinger, J. C. et al. Conformation and energy transfer in single conjugated polymers. *Acc. Chem. Res.* **45**, 1992–2001 (2012).
119. Feist, F. A. & Basché, T. The folding of individual conjugated polymer chains during annealing. *Angew. Chem. Int. Ed.* **50**, 5256–5257 (2011).
120. Lee, S. H. et al. Investigation and control of single molecular structures of meso–meso linked long porphyrin arrays. *J. Phys. Chem. B* **122**, 5121–5125 (2018).
121. Würsch, D. et al. Molecular water lilies: Orienting single molecules in a polymer film by solvent vapor annealing. *J. Phys. Chem. Lett.* **7**, 4451–4457 (2016).
122. Tenopala-Carmona, F., Fronk, S., Bazan, G. C., Samuel, I. D. W. & Penedo, J. C. Real-time observation of conformational switching in single conjugated polymer chains. *Sci. Adv.* **4**, eaao5786 (2018).
123. Joung, H. et al. Impact of chain conformation on structural heterogeneity in polymer network. *Nano Lett.* **22**, 5487–5494 (2022).